JACS
JOURNAL OF THE AMERICAN CHEMICAL SOCIETY
Article
Cite This: J. Am. Chem. Soc. 2017, 139, 16591-16603
pubs.acs.org/JACS

Multi-Stage Structural Transformations in Zero-Strain Lithium Titanate Unveiled by *in Situ* X-ray Absorption Fingerprints

Wei Zhang,[†,⊗] Mehmet Topsakal,[‡,⊗] Christina Cama,[§] Christopher J. Pelliccione,[∥] Hu Zhao,[†] Steven Ehrlich,[□] Lijun Wu,[⊥] Yimei Zhu,[⊥] Anatoly I. Frenkel,[#,▽] Kenneth J. Takeuchi,[§,▽] Esther S. Takeuchi,[§,▽,∥] Amy C. Marschilok,[*,§,▽,∥] Deyu Lu,[*,‡] and Feng Wang[*,†]

[†]Sustainable Energy Technologies Department, Brookhaven National Laboratory, Upton, New York 11973, United States
[‡]Center for Functional Nanomaterials, Brookhaven National Laboratory, Upton, New York 11973, United States
[§]Department of Chemistry, Stony Brook University, Stony Brook, New York 11794, United States
[∥]Energy and Photon Sciences Directorate, Brookhaven National Laboratory, Upton, New York 11973, United States
[⊥]Condensed Matter Physics and Materials Science Department, Brookhaven National Laboratory, Upton, New York 11973, United States
[#]Chemistry Department, Brookhaven National Laboratory, Upton, New York 11973, United States
[▽]Department of Materials Science and Chemical Engineering, Stony Brook University, Stony Brook, New York 11794, United States
[□]National Synchrotron Light Source II, Brookhaven National Laboratory, Upton, New York 11973, United States

Supporting Information

ABSTRACT: Zero-strain electrodes, such as spinel lithium titanate ($Li_{4/3}Ti_{5/3}O_4$), are appealing for application in batteries due to their negligible volume change and extraordinary stability upon repeated charge/discharge cycles. On the other hand, this same property makes it challenging to probe their structural changes during the electrochemical reaction. Herein, we report *in situ* studies of lithiation-driven structural transformations in $Li_{4/3}Ti_{5/3}O_4$ via a combination of X-ray absorption spectroscopy and *ab initio* calculations. Based on excellent agreement between computational and experimental spectra of Ti K-edge, we identified key spectral features as fingerprints for quantitative assessment of structural evolution at different length scales. Results from this study indicate that, despite the small variation in the crystal lattice during lithiation, pronounced structural transformations occur in $Li_{4/3}Ti_{5/3}O_4$, both locally and globally, giving rise to a multi-stage kinetic process involving mixed quasi-solid solution/macroscopic two-phase transformations over a wide range of Li concentrations. This work highlights the unique capability of combining *in situ* core-level spectroscopy and *first-principles* calculations for probing Li-ion intercalation in zero-strain electrodes, which is crucial to designing high-performance electrode materials for long-life batteries.

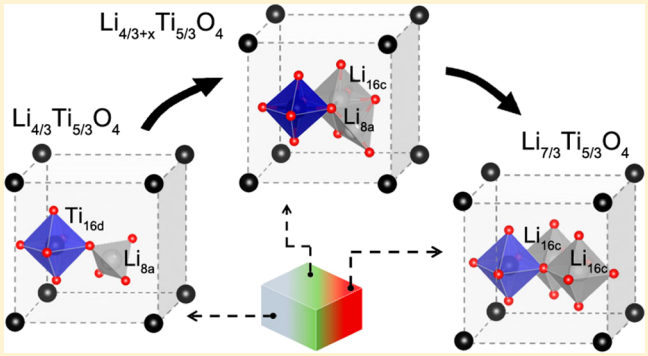

INTRODUCTION

Lithium-ion batteries (LIBs) have become the most widely used power sources for portable electronic devices, and their use in electric vehicles (EVs) and stationary storage is increasing rapidly with continuous improvement in energy density, safety, and lifetime.[1,2] For the specific application in long-life LIBs, "zero-strain" electrodes are attractive due to their characteristic small volume change during Li-ion intercalation, ensuring potentially long cycling stability. One representative is lithium titanate ($Li_{4/3}Ti_{5/3}O_4$), a well-known defective spinel anode (space group $Fd\bar{3}m$) with tetrahedral 8a sites occupied by Li and octahedral 16d sites randomly occupied by 1/6 Li and 5/6 Ti in the cubic-close-packed (*ccp*) O sublattice. It is generally believed that, during a normal discharge (above 1.0 V), $Li_{4/3}Ti_{5/3}O_4$ accommodates lithium *via* a two-phase transformation, from the initial spinel structure to a rock-salt-structured $Li_{7/3}Ti_{5/3}O_4$ (space group $Fm\bar{3}m$), with volume change of only ~0.2%.[3,4] In the $Li_{4/3}Ti_{5/3}O_4$-based electrodes, long cycling stability and fast rate capability have been demonstrated, highlighting the advantage of using zero-strain materials.[5−7] On the other hand, due to the zero-strain characteristics, experimental determination of the obscure structural evolution during Li intercalation has proven challenging, leaving a gap in fundamental understanding of the electrochemical processes in $Li_{4/3}Ti_{5/3}O_4$.

From the literature, the flat plateau in the (dis)charge voltage curves of $Li_{4/3}Ti_{5/3}O_4$ (at ~1.55 V) is commonly believed to be

Received: July 21, 2017
Published: October 13, 2017

DOI: 10.1021/jacs.7b07628
J. Am. Chem. Soc. 2017, 139, 16591−16603

an indicator of a macroscopic two-phase transformation, from $Li_{4/3}Ti_{5/3}O_4$ ($Li^{(8a)}[Li_{1/3}Ti_{5/3}]^{(16d)}O_4^{(32e)}$) to $Li_{7/3}Ti_{5/3}O_4$ ($Li_2^{(16c)}(Li_{1/3}Ti_{5/3})^{(16d)}O_4^{(32e)}$), and during the process all Li ions on tetrahedral 8a move to octahedral 16c sites, so that strain can be minimized.[8−13] However, because of the poor Li ion mobility in the two end-member phases, the macroscopic two-phase model is in conflict with the common experimental observation of high Li ion mobility in the electrodes at intermediate Li concentrations (namely, $Li_{4/3+x}Ti_{5/3}O_4$ with $0 < x < 1$).[14−17] Recent experimental and computational evidence attributed this puzzling behavior to the existence of intermediate $Li_{4/3+x}Ti_{5/3}O_4$ phase in which Li ions simultaneously occupy face-shared 8a and 16c sites.[13−15,18,19] However, there have been different proposals about the nature of the $Li_{4/3+x}Ti_{5/3}O_4$ phase: either a homogeneous solid solution[14] or a nanoscale phase separated system containing nanometer-sized end member domains along with abundant domain boundaries.[13,15,19] It is until recently that computational studies predicted the existence of metastable $Li_{4/3+x}Ti_{5/3}O_4$ with nearest Li_{8a}-Li_{16c} neighbors at the phase boundaries of $Li_{4/3}Ti_{5/3}O_4/Li_{7/3}Ti_{5/3}O_4$, facilitated by the presence of the defective Li_{16d} ions.[19]

Despite significant progress in developing *in situ* characterization techniques in recent years,[20] experimental determination of the local structure in the intermediates ($Li_{4/3+x}Ti_{5/3}O_4$) has been challenging due to technical difficulties in distinguishing structural configurations or Li site occupancy in $Li_{4/3+x}Ti_{5/3}O_4$ (of varying Li cocentration, x).[3,4,12,13,21] For example, measurements using Li-sensitive nuclear magnetic resonance (NMR) techniques provided convincing evidence of Li site occupancy on both tetrahedral (8a) and octahedral (16d) sites in the pristine $Li_{4/3}Ti_{5/3}O_4$.[22] However, determination of Li migration by NMR becomes especially challenging because of interference of the local magnetic ordering with the measure of resonance in the lithiated $Li_{4/3+x}Ti_{5/3}O_4$.[23] X-ray absorption spectroscopy (XAS) has been widely applied to characterizing electrode materials.[24−28] Detailed information about the electronic structures and local atomic arrangements around Ti in various Ti-containing materials was obtained from the XAS near edge structure (XANES).[25−29] Since Li insertion alters the charge distribution around neighboring O and Ti ions in $Li_{4/3}Ti_{5/3}O_4$,[30] the Ti−O bonds and the geometrical arrangement of atoms around Ti ions change correspondingly. In principle, such information can be extracted from the Ti K-edge XANES and further correlated to the kinetic pathway of Li-ion intercalation. Nevertheless, *in situ* Ti K-edge XAS has been scarcely applied to studying Li intercalation in $Li_{4/3}Ti_{5/3}O_4$, because of the difficulty in acquiring the spectra at a low energy range (below 5 keV) from general *in situ* electrochemical cells.[21,31] On the theory side, spectral interpretation of the Ti K-edge XANES spectra of $Li_{4/3}Ti_{5/3}O_4$ *via ab initio* electronic structure calculations is largely missing in the literature.[29]

In this work, *in situ* electrochemical cells were designed, with configurations allowing for measuring Ti K-edge XAS spectra under fluorescence mode during electrochemical cycling of $Li_{4/3}Ti_{5/3}O_4$ electrodes. Owing to the high structure reversibility of $Li_{4/3}Ti_{5/3}O_4$ during repeated charge/discharge cycles,[4,32,33] we focused our studies on the first discharge process. State-of-the-art *ab initio* calculations were carried out to model the atomic structure and the Ti K-edge XANES. Main spectral features were well reproduced by theory, which allowed us to identify the origins of spectral changes in the Ti K-edge XANES spectra in terms of reduction of the Ti^{4+} to Ti^{3+}, local distortion of the TiO_6 octahedra, and the Li occupancy at different sites during Li-ion intercalation. These spectral features were then employed as fingerprints for quantitative assessment of the structural transformations in $Li_{4/3}Ti_{5/3}O_4$. Results from this study indicate a multi-stage kinetic process, involving a mixed quasi-solid solution and the macroscopic two-phase transformations over a wide range of Li concentrations. The developed approach based on XAS spectral fingerprints may be broadly applicable to studies of various electrode materials to obtain quantitative information essential to the description of their kinetic electrochemical pathways.

EXPERIMENTS AND CALCULATIONS

Electrochemical and Structural Characterization. The $Li_{4/3}Ti_{5/3}O_4$ powders were obtained from nGimat Company. The electrodes used in general coin cells were prepared by mixing 60 wt% $Li_{4/3}Ti_{5/3}O_4$, 20 wt% Super P carbon, and 20 wt% polyvinylidene fluoride (PVDF). Thirty-micrometer-thick electrodes were coated onto a copper foil current collector and dried under vacuum at 120 °C for 8 h. All cells were assembled in an Ar glovebox with standard electrolyte of ethylene carbonate (EC)/dimethyl carbonate (DMC)/$LiPF_6$ (1:1:1) and Li metal as the counter-electrode. The coin cells were electrochemically cycled under the galvanostatic condition between 2.50 and 1.00 V at a rate of C/10. Annular dark-field (ADF) images and high-angle annular dark-field (HAADF) images were recorded in a JEOL ARM 200F microscope equipped with two spherical-aberration correctors and a cold-field-emission electron source.

***In Situ* and *Ex Situ* XAS Measurements.** *In situ* XAS experiments were performed at beamline X18A of the National Synchrotron Light Source (NSLS) at Brookhaven National Laboratory (BNL). The *in situ* cells were constructed from conventional coin cells. A hole was punched in the stainless steel case of the bottom side of the cell and then sealed with Kapton tape (Kapton polyimide film with Silicone adhesive) to create an X-ray-transparent window. The electrode slurry was cast on an aluminum mesh current collector and placed over the Kapton window to maintain the electronic conduction between the electrode and the stainless steel case. The X-ray beam was incident over a ~1 × 1 mm^2 area of the electrode, and the spectra were recorded in fluorescence mode using a passivated implanted planar silicon (PIPS) detector while the electrode was discharged at a rate of C/10 (see Figure 2a for the illustration). The *ex situ* XAS measurements were collected at the Ti K edge on $Li_{4/3}Ti_{5/3}O_4$ electrodes that were discharged to 3.00, 1.60, and 1.00 V, respectively. All XAS spectra were aligned, merged, deglitched, and normalized using Athena software.[34,35] High consistency in background subtraction ensured that no artifacts came from data analysis (as shown in Figure S1). The multi-peak fits were carried out to simultaneously fit the pre-edge peaks A, B, and C to three Gaussian functions, which provided the peak area and corresponding standard deviation for every pre-edge peak (called pre-peak henceforth).

***In Situ* XRD Measurements.** *In situ* electrochemical cells for XRD measurements were constructed similarly to the *in situ* XAS measurements, except that holes were drilled in both sides of the cell so that X-rays can pass through the cell. A 10 nm Cu film was deposited onto the inner side of the window (by electron beam evaporation) to ensure good electronic connection for the electrode in the region over the window and the current collector. Experiments were performed at beamline X7B of the NSLS at BNL. Diffraction patterns were collected in transmission mode at a wavelength of 0.3184 Å. Hundreds of patterns were acquired to monitor the subtle structural changes occurring during the first discharge, which was performed at a C/10 rate. The data were acquired by a charge-coupled device (CCD) with 60 patterns averaged at each time interval, to ensure a good signal-to-noise ratio (SNR) in the high-angle region of the data, which is important for resolving the small volume changes. A

DOI: 10.1021/jacs.7b07628
J. Am. Chem. Soc. 2017, 139, 16591−16603

Si standard was employed to calibrate the sample-to-detector distance, the detector tilt angle of rotation, and the zero position.

Computation. Structural and electronic properties of $Li_{4/3+x}Ti_{5/3}O_4$ (x = 0, 1/6, and 1) were studied with the state-of-the-art *ab initio* methods. Structural optimizations were carried out with density functional theory (DFT) using the Heyd−Scuseria−Ernzerhof (HSE06) hybrid functional[36−38] and the projector augmented wave (PAW) method,[39] implemented in the *Vienna Ab Initio Simulation Package* (VASP).[40,41] While the density of states of $Li_{4/3}Ti_{5/3}O_4$ were calculated under the local density approximation (LDA), the LDA+U_{eff} method[42] was used to localize Ti 3d electrons in Ti^{3+} in the ground state of $Li_{4/3+x}Ti_{5/3}O_4$ and $Li_{7/3}Ti_{5/3}O_4$ with U_{eff} = 4.0 eV, consistent with reported values of 3.3−5.0 eV.[43−45] The kinetic energy cutoff of the plane-wave basis was chosen as 500 eV, and the Brillouin zone was sampled with a 4×4×2 Γ-centered grid for all the systems, because their lattice vectors from HSE06 are within 0.13%. Ti K-edge XANES spectra were calculated at the HSE06 equilibrium structures at zero temperature using the *Obtaining Core Excitations from Ab initio Electronic Structure and NBSE* (OCEAN) package.[46,47] Ground-state wave functions and orbital energies, which are input for OCEAN calculations, were obtained from plane-wave norm-conserving (NC) pseudopotential calculations using Quantum ESPRESSO[48] with a kinetic energy cutoff of 100 Ry. We have verified that the total density of states (DOS) of $Li_{4/3}Ti_{5/3}O_4$ from VASP and Quantum ESPRESSO are almost identical, as shown in Figure S2. The final state effects are included through the effective electron - core hole interaction, treated by the Bethe−Salpeter equation (BSE). A total of 1200 bands were included (about 100 eV above the Fermi level) to compute the screened core-hole potential in OCEAN calculations. For better comparison with experimental spectra, the OCEAN spectra were post-processed with a Gaussian broadening (σ = 0.2 eV) followed by energy dependent Lorentzian broadening. Full width at half-maximum (fwhm) of Lorentzian broadening was chosen as $(E - E_{onset})/10$, with E_{onset} being the onset energy of the calculated spectra.[49]

The procedure to align computational XANES spectra with experimental spectra is not straightforward, because the absolute core level energies cannot be obtained directly from the pseudopotential-based method. In order to align OCEAN spectra with experimental spectra, the OCEAN spectrum of each Ti was shifted by ΔE according to the relation, $\Delta E = \Delta E_0 + \Delta E_{1s}$, where ΔE_0 is a site-independent energy shift of the reference system, $Li_{4/3}Ti_{5/3}O_4$. ΔE_0 = 4959.7 eV was used to align the second pre-edge peak of $Li_{4/3}Ti_{5/3}O_4$ of the OCEAN spectrum with the experimental spectrum. ΔE_{1s} is the relative 1s core-level shift for each Ti with respect to averaged 1s core-level energy of $Li_{4/3}Ti_{5/3}O_4$. In each system, Ti 1s core-level energies were determined from the Kohn−Sham (V_{KS}) and static Coulomb-hole potentials (W_c) in a fully *ab initio* procedure.[50]

RESULTS AND DISCUSSION

Lithiation-Driven Structural Evolution. Figure 1 presents the structural and electrochemical characterization of $Li_{4/3}Ti_{5/3}O_4$ samples (consisting of nanoparticles). The $Li_{4/3}Ti_{5/3}O_4$ nanoparticles generally possess a plate-like morphology with average particle size around 200 nm (Figure 1a). The atomic arrangement in the spinel structure (space group: $Fd\bar{3}m$) was determined using HAADF imaging projected along the [110] direction (Figure 1b). The Ti ions at 16d sites were clearly resolved in the HAADF image, which is consistent with the structural model in Figure 1c. In addition, the atomic column 1 has brighter contrast than the atomic column 2, because column 1 has twice the number of Ti ions as in column 2. However, uniform contrast is displayed for both these columns in Figure 1b, which indicates a random distribution of Li ions throughout the 16d sites.

Following galvanostatic cycling between 2.50 and 1.00 V, a flat voltage plateau at ∼1.55 V was observed, indicating a two-phase transformation between the spinel-structured

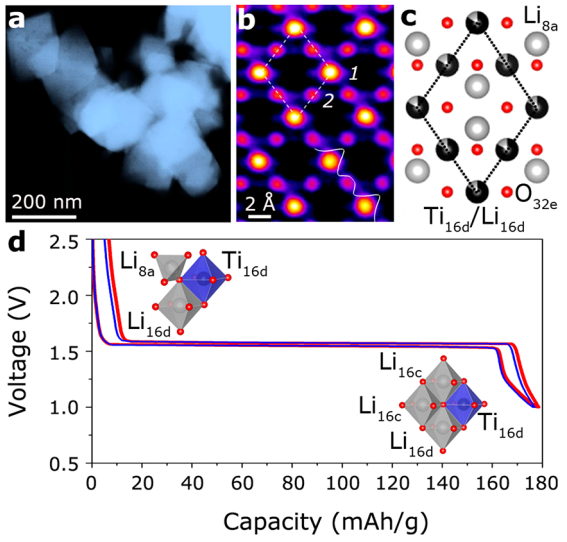

Figure 1. Structure and electrochemical properties of lithium titanate. (a) Annular dark-field (ADF) image showing a plate-like morphology of $Li_{4/3}Ti_{5/3}O_4$ nanoparticles. (b) High-angle ADF image showing highly ordered spinel structure projected along the [110] direction. Labels 1 and 2 in (b) are used to distinguish two atomic columns with different Ti occupancies, therefore giving rise to different intensities, as shown by the inxtensity profile (inset). (c) Structure model illustrating the Ti, Li, and O occupancy in a unit cell of the spinel structure, also marked by the white dashed lines in (b). (d) Voltage profiles for the first (red curve) and second (blue curve) cycles of $Li_{4/3}Ti_{5/3}O_4$ electrodes, being galvanostatically discharged/charged between 2.50 and 1.00 V at a rate of C/10. The Li and Ti occupancies in the pristine ($Li_{4/3}Ti_{5/3}O_4$) and fully discharged ($Li_{7/3}T_{5/3}O_4$) are illustrated in the inset, with Li occupying 8a/16d sites in the former and 16c/16d sites in the latter.

$Li_{4/3}Ti_{5/3}O_4$ and the rock-salt-structured $Li_{7/3}Ti_{5/3}O_4$. During this process, Li migrates between 8a and 16c sites (Figure 1d).[4,12] The structural change in $Li_{4/3}Ti_{5/3}O_4$ electrodes during discharge between 2.50 and 1.00 V at 0.1 C was measured by *in situ* XRD (Figure S3). Owing to negligible change in lattice parameters between the pristine and lithiated phases (below 0.1%), a high-angle scattering peak at around 21.9° (being indexed to (177), was used for identifying phase evolution. At lithium concentration $x \approx 0.13$, a new peak associated with $Li_{7/3}Ti_{5/3}O_4$ phase, emerges on the right side of the peak and grows gradually with x, indicating an overall two-phase transformation. However, the high similarity in the positions of the two peaks makes it very difficult to identify any additional peaks associated with other phases between $Li_{4/3}Ti_{5/3}O_4$ and $Li_{7/3}Ti_{5/3}O_4$.

To identify the detailed structural evolution in $Li_{4/3}Ti_{5/3}O_4$ during discharge, we performed *in situ* XAS measurements on $Li_{4/3}Ti_{5/3}O_4$ electrodes, as shown in Figure 2. The experimental setup for *in situ* XAS measurements in the fluorescence mode is illustrated in Figure 2a (see detailed information in Experiments and Calculations). Ti K-edge XAS spectra were collected at an interval of Li concentration x = 0.067 per spectrum during lithiation (Figure 2b). The spectral features of the *in situ* data are comparable to that of *ex situ* XAS measurements on several $Li_{4/3}Ti_{5/3}O_4$ electrodes discharged to different levels of Li concentration (Figure S4). In the pristine state, three pre-peaks (A, B, and C) and two main edge peaks D and E are evident in the Ti K-edge XANES spectrum, at 4968, 4971, 4974, 4990, and 5002 eV, respectively (Figure 2b). During the whole

DOI: 10.1021/jacs.7b07628
J. Am. Chem. Soc. 2017, 139, 16591−16603

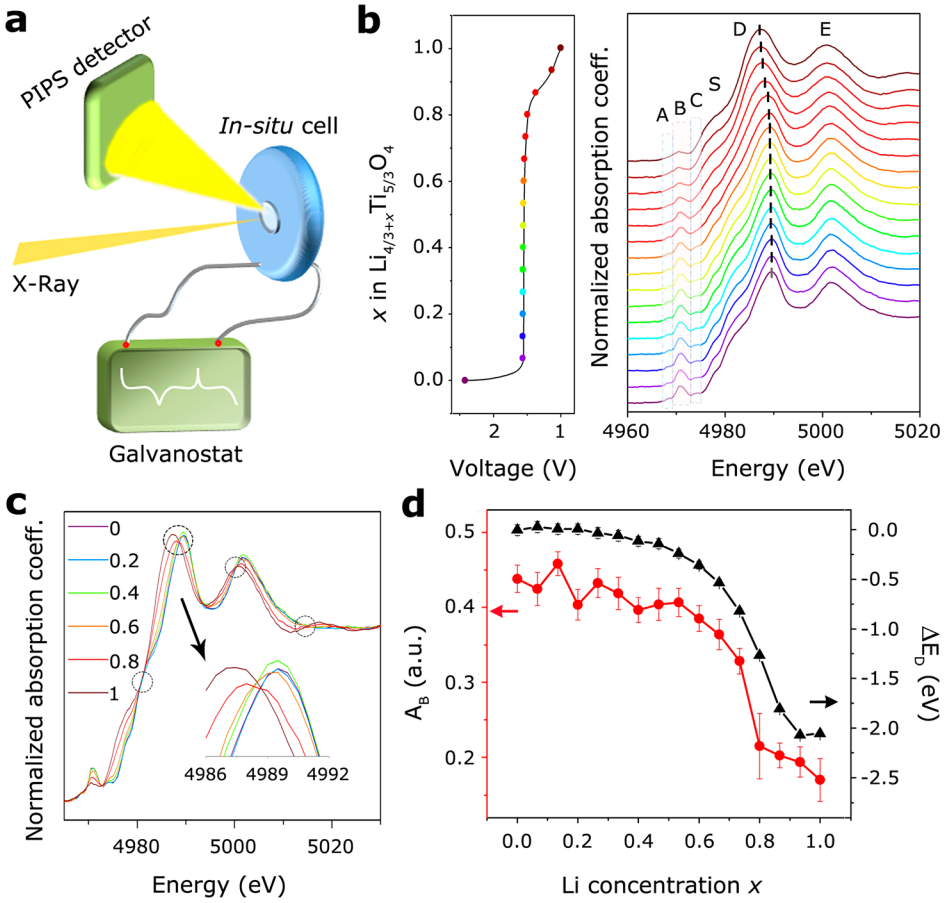

Figure 2. Tracking of structural evolution in lithium titanate electrodes via *in situ* X-ray absorption spectroscopy (XAS). (a) Schematic illustration of the setup for *in situ* XAS measurements in fluorescence mode. The electrode was discharged against Li metal counter electrode in an *in situ* cell using a galvanostat, with X-ray beam incident over a ~1 × 1 mm^2 area of the electrode. The fluorescence signal was collected using a passivated implanted planar silicon (PIPS) detector sitting close to the window of the cell. (b) Series of Ti K-edge XAS near-edge spectra (XANES) as a function of Li concentrations (x), recorded from $Li_{4/3}Ti_{5/3}O_4$ electrode during the first lithiation under galvanostatic mode at a rate of 0.1 C. The states of lithiation corresponding to individual spectra are labeled in the voltage profile using colored dots (left). Major features of the spectra are labeled by letters A, B, C (for the three peaks in the pre-edge region), S (the peak on the shoulder, shown up in the deep lithiation stage), D, and E (the two main edge peaks). The position of peak D in each spectrum of the series is marked using a black dashed line, showing a gradual red-shift as lithiation progresses. (c) Selected XANES spectra showing quasi-isosbestic points as marked by black dashed circles. Zoom-in view of one representative of the quasi-isosbestic points is given in the inset, displaying a roughly defined isosbestic point. (d) Area of the pre-peak B (defined as A_B) and relative shift of peak D (defined as $\Delta E_D = E(x) - E(0)$, where $E(x)$ and $E(0)$ are the energy positions of peak D corresponding to $Li_{4/3+x}Ti_{5/3}O_4$ and $Li_{4/3}Ti_{5/3}O_4$, respectively) as a function of Li concentration x. The error bars represent standard deviations extracted from fitting of pre-peak B using a Gaussian function.

discharge process, the position of peak E does not change. The main peak D red-shifts from $Li_{4/3}Ti_{5/3}O_4$ to $Li_{7/3}Ti_{5/3}O_4$, which is an indication of the partial reduction of Ti^{4+} to Ti^{3+}. In addition, fine spectral features (i.e., small shoulders in the arising edge) in the range between 4976 and 4980 eV are gradually broadened, becoming barely discernible after x = 0.5, and eventually evolve into a new broad peak S, at ~4978 eV (Figure 2b).

Furthermore, three predominant features of spectral evolution in the *in situ* XANES should be noted. First, the *in situ* XANES spectra display quasi-isosbestic points at around 4981, 4988, 5000, and 5014 eV, where curves do not share a single point (as illustrated by the inset in Figure 2c), in contrast to real isosbestic points observed in other two-phase reaction electrodes.[51] Second, significant spectral changes were found in the pre-edge region, revealed by the evolution of the area of these pre-peaks obtained through Gaussian fitting (Figure S5). Overall the area of pre-peak A remains constant (within the error of fitting), while the area of pre-peak C continuously decreases until Li concentration x = 1.0 (Figure S6). The change in the area of pre-peak B (defined as A_B) is much more pronounced. Overall, it decays slowly below x = 0.5, drops abruptly afterward until x = 0.87, and then slows down again until x = 1.0 (Figure 2d). Third, a similar trend was observed during the redshift of peak D, defined by $\Delta E_D = E(x) - E(0)$, where $E(x)$ and $E(0)$ are the positions of peak D in the spectra of intermediate and pristine states, respectively (Figure 2d). The peak D only slightly shifts by −0.2 eV (from 4989.5 to 4989.3 eV) before x = 0.5, followed by a significant shift of −1.6 eV to $E(0.87)$ = 4987.7 eV, and then undergoes a slow shift of −0.3 eV to $E(1)$ = 4987.4 eV until x = 1.0 (Figure 2d).

Kinetic Transformation Pathway. The *in situ* XAS spectra were further analyzed to gain insight into the kinetic phase evolution during the Li intercalation process. A standard technique to determine the first-order phase transformation is to fit the spectra of intermediates to a linear combination of the spectra of the two end members. Such linear fitting has been widely used in the literature. For example, the two-phase

DOI: 10.1021/jacs.7b07628
J. Am. Chem. Soc. 2017, 139, 16591−16603

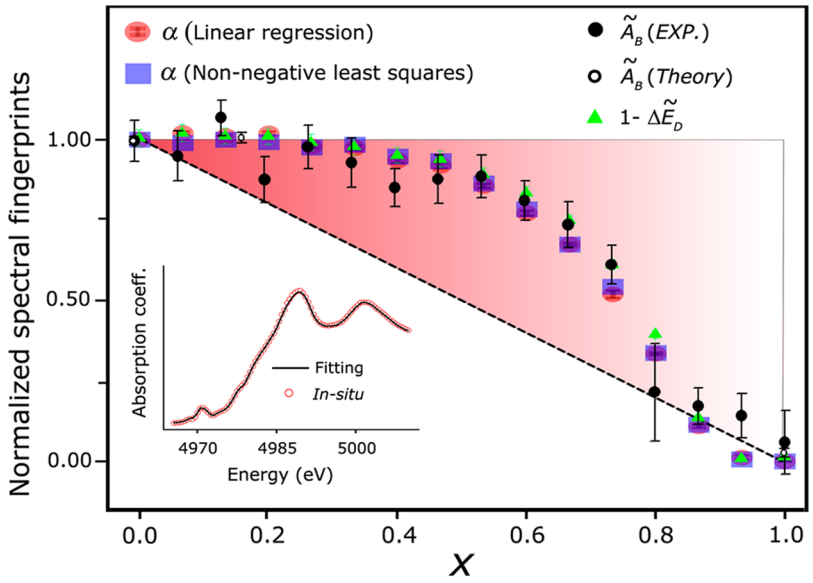

Figure 3. Evolution of the spectral weight of $Li_{4/3}Ti_{5/3}O_4$ phase against normalized amplitude of spectral fingerprints (area of the pre-peak B and shift of the main peak D) during Li intercalation in lithium titanate. Two-phase transformation line (black dashed) refers to the ideal condition, $\alpha_0(x) = 1 - x$, in which the weight of the $Li_{4/3}Ti_{5/3}O_4$ phase $\alpha_0(x)$ linearly decreases as lithiation progresses. Pink dots and violet squares represent weight of the $Li_{4/3}Ti_{5/3}O_4$ phase, $\alpha(x)$, obtained using linear regression (LR) fitting and non-negative least-squares (NNLS) methods, respectively. The inset demonstrates good fitting of the XANES spectrum from one intermediate ($x = 0.6$), with $\alpha = 0.77$ and error bar of ± 0.01, using LR method. For comparison, the normalized area of pre-peak B from experiments, $\tilde{A}_B(x)$ (black solid circles), and from calculated spectra of $Li_{4/3}Ti_{5/3}O_4$, $Li_{4.5/3}Ti_{5/3}O_4$, and $Li_{7/3}Ti_{5/3}O_4$, $\tilde{A}_B(x)$ (black open circles), along with the normalized shift of peak D (green triangle), are also plotted as a function of x, indicating a direct correlation to $\alpha(x)$. Here, $\tilde{A}_B(x)$ is defined by $\tilde{A}_B(x) = (A_B(x) - A_B(1))/(A_B(0) - A_B(1))$, where $A_B(0)$, $A_B(x)$, and $A_B(1)$ are the areas of pre-peak B corresponding to the $Li_{4/3}Ti_{5/3}O_4$, $Li_{4/3+x}Ti_{5/3}O_4$, and $Li_{7/3}Ti_{5/3}O_4$, respectively, obtained from *in situ* XAS spectra. The normalized shift of the main peak D is defined as $1 - \Delta\tilde{E}_D(x) = 1 - \Delta E_D(x)/\Delta E_D(1)$, where $E(1)$ is the position of peak D corresponding to $Li_{7/3}Ti_{5/3}O_4$. Both theoretical and experimental values of the pre-peak B areas at $x = 0.0$ have been normalized to 1.0. The error bars represent standard deviations extracted from Gaussian function.

transformation of $LiFePO_4$ during lithiation was confirmed by fitting the P K-edge XAS of intermediates with the linear combination of the spectra of $FePO_4$ and $LiFePO_4$.[52] Principal component analysis on *in situ* XAS spectra of $Li_{4/3+x}Ti_{5/3}O_4$ yields two dominant components originated from the spectra of two end members, which justifies the linear combination approach. We applied linear regression (LR) to fit the spectra of intermediates ($Li_{4/3+x}Ti_{5/3}O_4$) to a linear combination of the spectra of the two end members ($Li_{4/3}Ti_{5/3}O_4$ and $Li_{7/3}Ti_{5/3}O_4$), with the spectral weight of $Li_{4/3}Ti_{5/3}O_4$ denoted by $\alpha(x)$. Exemplary LR fitting of *in situ* XAS at $x = 0.6$ is shown in the inset of Figure 3, and results at different x are provided in Figure S7. The non-negative least-squares method (NNLS)[53] was used to verify the robustness of the LR fitting, where weights of $Li_{4/3}Ti_{5/3}O_4$ and $Li_{7/3}Ti_{5/3}O_4$ spectra were restricted to be positive. Except for small deviations in $0 < x \leq 0.26$, overall very good agreement of the results between the LR and the NNLS methods and between fitting and experimental curves suggests that the numerical fitting is robust. In addition, we have applied the multivariate curve resolution−alternating least squares (MCR-ALS)[54−56] method, which employs spectral deconvolution to find pure components present in the series of measured spectra. Evolution of normalized concentration of the first component (representing $Li_{4/3}Ti_{5/3}O_4$) from MCR-ALS analysis agrees with the LR and NNLS analysis with further details in Note S1 and Figure S8.

The evolution of $\alpha(x)$ as a function of x is shown in Figure 3. The two-phase transformation line is referred to as $\alpha_0(x) = 1 - x$, in which the weight of $Li_{4/3}Ti_{5/3}O_4$ phase decreases linearly as x increases. Only on $\alpha_0(x)$, the spectral weight, $\alpha(x)$, coincides with the percentage of the $Li_{4/3}Ti_{5/3}O_4$ domains. Instead, $\alpha(x)$ exhibits non-linear characteristics with multiple slopes, indicating multi-stage structural transformations during the Li intercalation process. At low concentrations ($x \leq 0.5$), $\alpha(x)$ decreases slightly to about 0.92, showing almost a flat plateau. At the range of $0.5 \leq x \leq 0.87$, $\alpha(x)$ drops rapidly to about 0.1. $\alpha(x)$ intersects with $\alpha_0(x)$ at $x = 0.87$ and follows $\alpha_0(x)$ until $x = 1.0$, indicating that the system rapidly segregates into two macroscopic phases. Evidently the structural transformations under the *in situ* condition cannot be simply described by a macroscopic two-phase transformation alone, as $\alpha(x)$ deviates significantly from the two-phase transformation line for most of the intermediate concentrations.

In order to analyze the characteristic non-linear trend of $\alpha(x)$, we examined two spectral fingerprints associated with the area of pre-peak B and the shift of peak D. Their values were normalized for the convenience of comparison with $\alpha(x)$; namely, for the area of pre-peak B, $\tilde{A}_B(x) = (A_B(x) - A_B(1))/(A_B(0) - A_B(1))$; and for the shift of peak D, $1 - \Delta\tilde{E}_D(x) = 1 - \Delta E_D(x)/\Delta E_D(1)$. From Figure 3, one can clearly see that these two spectral fingerprints and $\alpha(x)$ fall onto a universal curve, despite their rather different nature. This universal behavior suggests that the underlying electronic and structural properties related to $\tilde{A}_B$ and $\Delta\tilde{E}_D$ are intimately correlated with the evolution of $\alpha(x)$, and, therefore, $\tilde{A}_B$ and $\Delta\tilde{E}_D$ are the keys to unveiling the multi-stage evolution during lithiation in $Li_{4/3}Ti_{5/3}O_4$.

Spectral Interpretation via First-Principles Calculations. In order to interpret the main spectral changes in $Li_{4/3}Ti_{5/3}O_4$ in terms of the structural transformations, *ab initio* calculations were carried out. Following Ziebarth et al.,[57] we modeled the atomic structure of $Li_{4/3}Ti_{5/3}O_4$ using a hexagonal

DOI: 10.1021/jacs.7b07628
J. Am. Chem. Soc. 2017, 139, 16591−16603

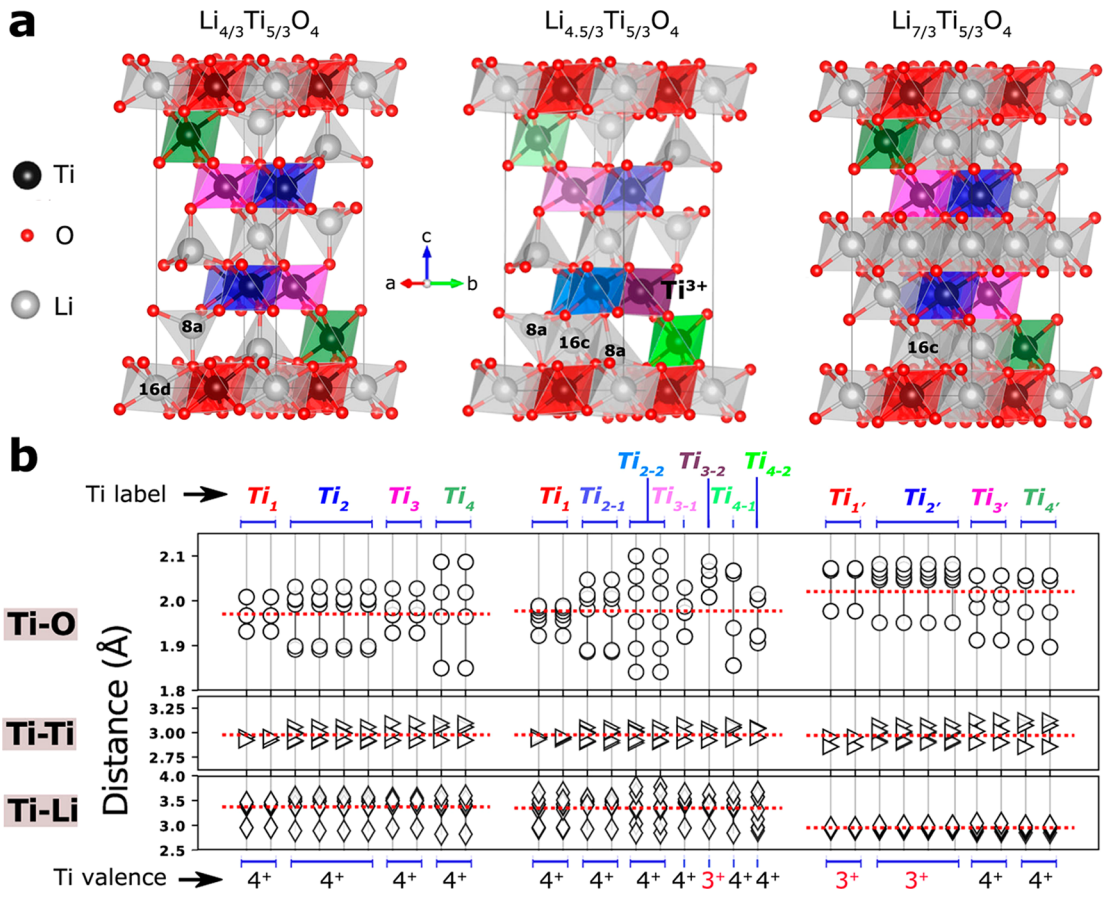

Figure 4. Structure models of lithium titanate used for *ab initio* calculations. (a) Atomic configurations of the spinel ($Li_{4/3}Ti_{5/3}O_4$) and rock-salt ($Li_{7/3}Ti_{5/3}O_4$), respectively, in the hexagonal unit cell (constructed in the same way as in ref 57), where Li^+ ions occupy 8a/16d and 16c/16d sites in former and latter cases. One possible configuration of an intermediate phase $Li_{4/3+x}Ti_{5/3}O_4$ (Li concentration $x = 0.166$; namely $Li_{4.5/3}Ti_{5/3}O_4$) is also given, showing that one Li^+ ion occupies a 16c site in $Li_{4.5/3}Ti_{5/3}O_4$, forming a face-shared $Li_{8a}/Li_{16c}/Li_{8a}$ configuration as labeled in the structure model, while a nearby Ti^{4+} ion is reduced to Ti^{3+}. Inequivalent octahedra of Ti_{16d} in $Li_{4/3}Ti_{5/3}O_4$, $Li_{4.5/3}Ti_{5/3}O_4$, and $Li_{7/3}Ti_{5/3}O_4$ are labeled with different colors. Small red spheres denote oxygen ions at 32e sites, and gray spheres are Li^+ ions at 8a, 16c, and 16d sites. (b) Distances of nearest-neighbors Ti−O, Ti−Ti, and Ti−Li in $Li_{4/3}Ti_{5/3}O_4$, $Li_{4.5/3}Ti_{5/3}O_4$, and $Li_{7/3}Ti_{5/3}O_4$. Dashed red lines indicate average distances. Inequivalent Ti ions possess different types of bonding distances, which are labeled with different colors, corresponding to the colors of TiO_6 octahedra in (a). The Ti valence state for each type of Ti ions is given at the bottom.

super cell containing six chemical formula equivalents of $Li_{4/3+x}Ti_{5/3}O_4$ as shown in Figure 4, with the z axis along the [111] direction. This model was chosen to construct a minimum super cell that satisfies the correct stoichiometry at the 16d sites, with random occupancy by 1/3 Li and 5/3 Ti atoms per formula unit (also consistent with the HAADF image in Figure 1b). The most stable configuration corresponds to the largest distance between Li_{16d} ions so that the electrostatic repulsion is minimized.[57] Based on the translational and rotational symmetry, Ti ions in $Li_{4/3}Ti_{5/3}O_4$ can be classified into four inequivalent types as shown in Figure 4a: Ti_1 (red), Ti_2 (blue), Ti_3 (pink), and Ti_4 (green). When Li ions are intercalated to $Li_{4/3}Ti_{5/3}O_4$, Li_{8a} ions migrate to the 16c sites with the locations of Ti_{16d} ions unaffected in $Li_{7/3}Ti_{5/3}O_4$. Similarly, $Ti_{1'}$, $Ti_{2'}$, $Ti_{3'}$, and $Ti_{4'}$ refer to inequivalent Ti sites in $Li_{7/3}Ti_{5/3}O_4$. As for the intermediate states, a fundamental question is when and how Li_{8a} ions migrate to the 16c sites. If the Li_{8a} migration happens in a global manner at an early lithiation stage, the intermediate state will be dominated by 16c sites. On the opposite side, if such a global migration happens rather late, the intermediate state will be dominated by 8a sites. It is likely that the behavior of the Li_{8a} migration strongly depends on the (dis)charge rate in a kinetic process. Nevertheless, in both scenarios, an important configuration would be Li ions simultaneously occupying both 8a and 16c sites. For this reason, we selected a simplest representative $Li_{4.5/3}Ti_{5/3}O_4$ configuration, corresponding to $x = 0.166$ as shown in Figure 4a (middle). In this configuration, only one Li ion is accommodated in this solid solution phase, occupying one of the 16c sites to form a face-shared $Li_{8a}/Li_{16c}/Li_{8a}$ motif. Consequently, one nearby Ti^{4+} ion (labeled by the dark purple octahedron) is reduced to Ti^{3+}. More systematic studies of the configurations of the intermediates will be presented elsewhere.[58] Nevertheless, face-shared Li_{8a}/Li_{16c} is a common local structural feature in solid-solution $Li_{4/3+x}Ti_{5/3}O_4$.

The lattice constant changes very little from $Li_{4/3}Ti_{5/3}O_4$ (a = 5.907 Å and c = 14.470 Å) to $Li_{7/3}Ti_{5/3}O_4$ (a = 5.910 Å and c = 14.435 Å), in agreement with previous experimental and computational studies.[4,57] However, Ti−O, Ti−Ti, and Ti−Li distances undergo significant and non-uniform changes for inequivalent Ti ions upon Li intercalation, as a result of distinct atomic environment around the Ti 16d ions (Figure 4b). This is in contrast to an ideal perovskite structure, such as cubic $SrTiO_3$, where Ti−O, Ti−Ti, and Ti−Sr distances are equal for all Ti^{4+} ions. Ti_1 has three different Ti−O bond lengths, whereas Ti_2, Ti_3, and Ti_4 have four different Ti−O bond

DOI: 10.1021/jacs.7b07628
J. Am. Chem. Soc. 2017, 139, 16591−16603

lengths in $Li_{4/3}Ti_{5/3}O_4$. The variation of the Ti−O bond length is the largest for Ti_4, ranging from 1.85 to 2.09 Å. Previous DFT calculations with the Perdew−Burke−Ernzerhof (PBE) functional[59] yield a similar Ti−O bond length range, from 1.91 to 2.10 Å.[60] The average Ti−O bond length in $Li_{4/3}Ti_{5/3}O_4$ is 1.97 Å, and it increases to 2.02 Å in $Li_{7/3}Ti_{5/3}O_4$. The increase is mainly due to $Ti_{1'}$−O and $Ti_{2'}$−O bond length elongation (Figure 4b) that involves Ti^{3+} ions forming significantly weakened Ti−O bonds. As a result of Li_{8a} migration to Li_{16c} in $Li_{7/3}Ti_{5/3}O_4$, the Ti−Li distances are significantly modified as shown in the bottom stripe of Figure 4b. In $Li_{4/3}Ti_{5/3}O_4$, shorter Ti−Li distances of Ti_1, Ti_2, Ti_3, and Ti_4 (around 2.9 Å) are from Li_{16d}, while longer Ti−Li distances (around 3.5 Å) are from Li_{8a}. Average Ti−Li distance decreases from 3.37 in $Li_{4/3}Ti_{5/3}O_4$ to 2.95 Å in $Li_{7/3}Ti_{5/3}O_4$, because of short Ti−Li_{16d} and Ti−Li_{16c} distances in $Li_{7/3}Ti_{5/3}O_4$ upon the migration of Li_{8a} to Li_{16c}. However, the average Ti−Ti distance in $Li_{7/3}Ti_{5/3}O_4$ is almost unchanged compared to that in $Li_{4/3}Ti_{5/3}O_4$.

The insertion of one Li ion into 16c site leads to more heterogeneity of Ti−O and Ti−Li distances of inequivalent Ti ions in $Li_{4.5/3}Ti_{5/3}O_4$ (Figure 4b; middle). For example, the Ti_2−O, Ti_3−O, and Ti_4−O bond lengths are separated into two types, $Ti_{2-1}/Ti_{3-1}/Ti_{4-1}$ and $Ti_{2-2}/Ti_{3-2}/Ti_{4-2}$. While Ti−O bonding patterns in the first group are similar to those in $Li_{4/3}Ti_{5/3}O_4$, the second group exhibits significantly different Ti−O bonding patterns. These changes are induced by local distortions caused by the insertion of Li_{16c} and the change of Ti charge state, as Ti_{2-2}, Ti_{3-2}, and Ti_{4-2} are close to the face-shared $Li_{8a}/Li_{16c}/Li_{8a}$ motif, and Ti_{2-2} and Ti_{4-2} are close to the reduced Ti^{3+}_{3-2} ion (Figure 4b; middle). Notably, the Ti_{3-2}−O bond length is increased by 4% compared to Ti_3−O in $Li_{4/3}Ti_{5/3}O_4$, owing to the reduction of Ti_{3-2} ion. Therefore, the average Ti−O bond length is increased slightly from 1.97 Å in $Li_{4/3}Ti_{5/3}O_4$ to 1.98 Å in $Li_{4.5/3}Ti_{5/3}O_4$. The insertion of one Li ion in the 16c site modifies Ti−Li distances of surrounding Ti ions (mainly Ti_1, Ti_{2-2}, Ti_{3-2}, and Ti_{4-2} ions), causing the average Ti−Li distance to decrease slightly from 3.37 to 3.35 Å. However, the changes in Ti−Ti distance for all of the four types of Ti ions is small, and the change in the average Ti−Ti distance is negligible.

From the atomic structure analysis of the three systems in Figure 4, we conclude that while the Ti−O bond length is an indicator of the local distortion of the TiO_6 octahedra, it is the change in Ti−Ti distance that causes change to the lattice parameters. Therefore, the constant Ti−Ti distance during lithiation reflects the zero-strain nature of $Li_{4/3+x}Ti_{5/3}O_4$. On the other hand, the Ti−Li distance is more sensitive to the global structural changes, as Li_{8a} migrates to the 16c sites, than local distortions caused by the face-shared Li_{8a}/Li_{16c} motif.

In previous DFT studies, the ground state of $Li_{7/3}Ti_{5/3}O_4$ was treated as metallic.[19,61−64] While all Ti ions in $Li_{4/3}Ti_{5/3}O_4$ have the formal valence state of 4+, they are partially reduced to 3+ in $Li_{7/3}Ti_{5/3}O_4$ due to Li intercalation, resulting in partially filled Ti 3d bands. Spin-polarized HSE06 calculations yield the ground state with localized 3d electrons, 106 meV per Ti atom lower in energy than the itinerant configuration, consistent with the LDA+U_{eff} calculations (see Figure S9 for the density of states of the itinerant and the localized solution for Ti 3d states) and previous GGA+U_{eff} study.[43] Depending on the distribution of Ti^{3+} ions (6 out of 10 per supercell) in $Li_{7/3}Ti_{5/3}O_4$ (Figure 4a), there are many nearly degenerate spin configurations. The configuration in which Ti^{3+} ions are located on sites labeled by $Ti_{1'}$ and $Ti_{2'}$ is found to be energetically more favorable. We found that the ferromagnetic (FM) and various anti-ferromagnetic (AFM) configurations are only 3 meV different in energy per formula unit, with the FM configuration being the ground state. Due to such small energy differences, a mixture of magnetic ordering is expected at room temperature.

Experimental (*in situ*) Ti 1s XAS spectra ($Li_{4/3}Ti_{5/3}O_4$, $Li_{4.4/3}Ti_{5/3}O_4$, and $Li_{7/3}Ti_{5/3}O_4$) and computational (OCEAN) spectra ($Li_{4/3}Ti_{5/3}O_4$, $Li_{4.5/3}Ti_{5/3}O_4$, and $Li_{7/3}Ti_{5/3}O_4$) are presented in Figure 5a, showing the same characteristic features, pre-peaks (A, B, and C), main edge peaks (D and E), and the shoulder (S) between C and D. Good agreement between theory and experiment warrants accurate interpretation of the experimental spectra. In addition, atom and orbital projected density of states (PDOS) shown in Figure 5b were used to identify the electronic origin of the spectral features.

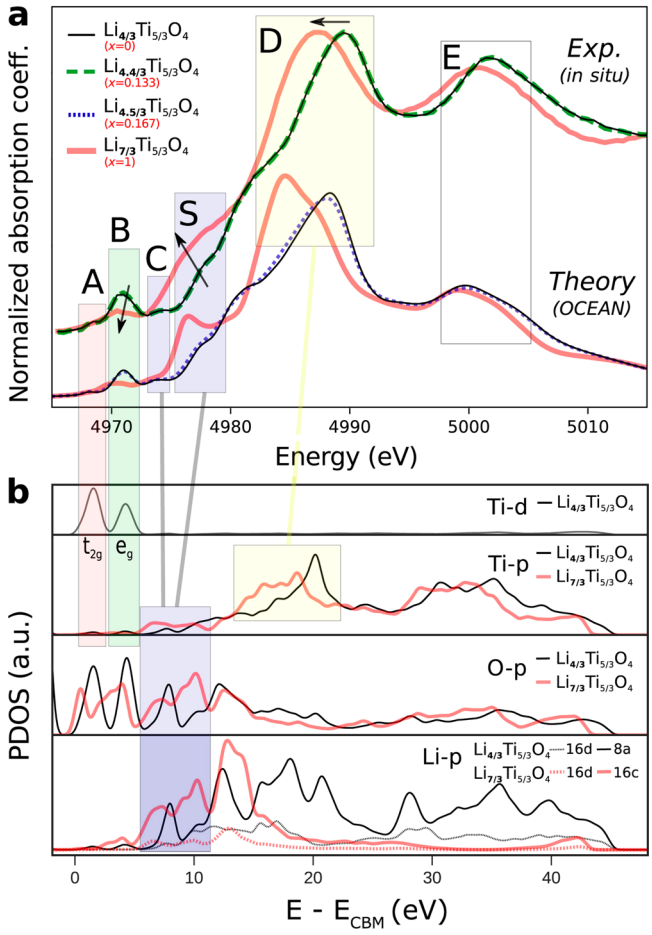

Figure 5. Calculated X-ray absorption near-edge spectra (XANES) of Ti K-edge and projected density of states (PDOS) for lithium titanate at different lithiated states. (a) Theoretical Ti K-edge XANES spectra in comparison to the experimental ones (from calculations using the OCEAN code and *in situ* measurements, respectively). Major features in the spectra are labeled by A, B, C, S, D, and E (defined the same as in Figure 2b). Black arrows highlight major changes of interest in the spectra. (b) Orbital and site projected conduction states of Ti, O, and Li, which were aligned with XANES spectra (shaded using the same colors). Zero of energy was set to the minimum of the conduction band (E_{CBM}). The Li-p PDOS peaks in the range of 5−11 eV are highlighted by dark gray, to show the direct correlation of the spectral changes to the Li migration between 8a and 16c sites.

DOI: 10.1021/jacs.7b07628
J. Am. Chem. Soc. 2017, 139, 16591−16603

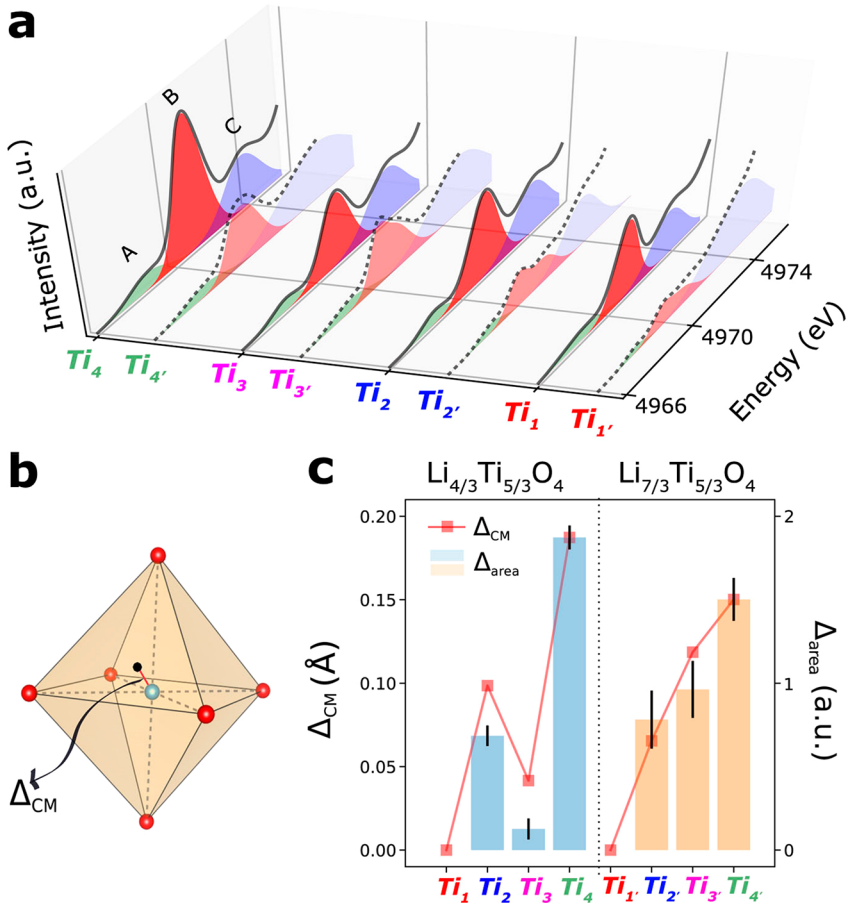

Figure 6. Correlation between the area of pre-peak B in the simulated Ti K-edge XAS and local distortion in lithium titanate. (a) Isolation of pre-peaks A, B, and C of inequivalent Ti atoms in $Li_{4/3}Ti_{5/3}O_4$ (denoted as T_n) and $Li_{7/3}Ti_{5/3}O_4$ ($T_{n'}$) using Gaussian functions. (b) Schematic illustration of the off-center displacement of Ti, wherein Δ_{CM} refers to the displacement distance of Ti ions from the center of mass (CM) in TiO_6 octahedra. (c) Variation of the displacement Δ_{CM} against area Δ_{area}, relative to that of T_1 and $T_{1'}$, indicating a nearly linear correlation (shown by the red line).

Pre-peaks A, B, and C are frequently observed in Ti compounds such as $SrTiO_3$ and $BaTiO_3$.[65−67] A and B correspond to the dipole-forbidden Ti 1s→3d (t_{2g} and e_g) transitions. However, dipolar contributions can arise from the hybridization of Ti t_{2g} and e_g states with ligand oxygen 2p states as shown in the PDOS in Figure 5b. Because e_g orbitals point toward surrounding oxygen atoms, the pre-peak B is sensitive to the local distortion of the TiO_6 octahedron. For example, A_B increases in Si(001)-supported $SrTiO_3$ upon the tetragonal distortion caused by the substrate.[65] Pressure-dependent studies of $BaTiO_3$ showed that A_B steadily decreases as the pressure increases from 2 to 10 GPa, as Ti ions move toward the center of the oxygen octahedron under higher pressure.[66] In another study on $BaTiO_3$, an empirical relation was reported between the area under the corresponding XANES peak in the 1s→3d transition region (A) and off-center displacement of Ti (d) by $A = \gamma d^2$, where γ denotes a system-dependent constant for a perovskite material.[67]

We found that pre-peaks A and B have a strong excitonic character, as the electron−core hole screened Coulomb interaction significantly modifies their oscillator strength, which was better captured by solving the BSE, as shown in Note S2 and Figure S10. This same trend has also been reported in simulations of Ti K-edge XANES from rutile TiO_2[68] and other transition metal compounds.[69−71] Pre-peak C has dipolar character from Ti-p states. Peaks D and E are also correlated with Ti-p states, i.e., the sharp peak at 20 eV and the broad peak at around 32 eV, respectively.

Several spectral changes reflect the evolution of the electronic structure and local bonding during Li intercalation. As shown in Figure 5a, pre-peak C is no longer visible in $Li_{7/3}Ti_{5/3}O_4$ especially with the rising intensity in the S region, and a new peak emerges in the calculated spectrum, consistent with the intensity increase of the experimental spectrum in the region. From the PDOS in Figure 5b, it is apparent that more Ti-p states are accumulated in the energy range from 5 to 11 eV in $Li_{7/3}Ti_{5/3}O_4$ than in $Li_{4/3}Ti_{5/3}O_4$. We can attribute this change to the occupation of Li_{16c} sites in $Li_{7/3}Ti_{5/3}O_4$. Because oxygen atoms initially bonded to Li_{8a} in $Li_{4/3}Ti_{5/3}O_4$ have now been bonded to Li_{16c} in $Li_{7/3}Ti_{5/3}O_4$, modified Li−O interaction affects the Ti−O interaction as revealed by the concerted changes of the O-p, Li-p, and Ti-p PDOS in the S region. Especially, the peaks between 5 and 11 eV in the Li_{8a} PDOS in $Li_{4/3}Ti_{5/3}O_4$ become broadened in $Li_{7/3}Ti_{5/3}O_4$ as shown in the Li_{16c} PDOS. Consequently, the growth of pre-peak S is an indicator of a global migration of Li from the 8a to 16c site, accompanied by the decrease of the average Ti−Li distances (as demonstrated in Figure 4b).

Another spectral change is the broadening and red-shift of main edge peak D (ΔE_D) from $Li_{4/3}Ti_{5/3}O_4$ to $Li_{7/3}Ti_{5/3}O_4$. A major factor that affects ΔE_D is the shift of the Ti 1s core levels (ΔE_{1s}), due to the reduction of Ti^{4+} to Ti^{3+}. Values of ΔE_{1s} of

DOI: 10.1021/jacs.7b07628
J. Am. Chem. Soc. 2017, 139, 16591−16603

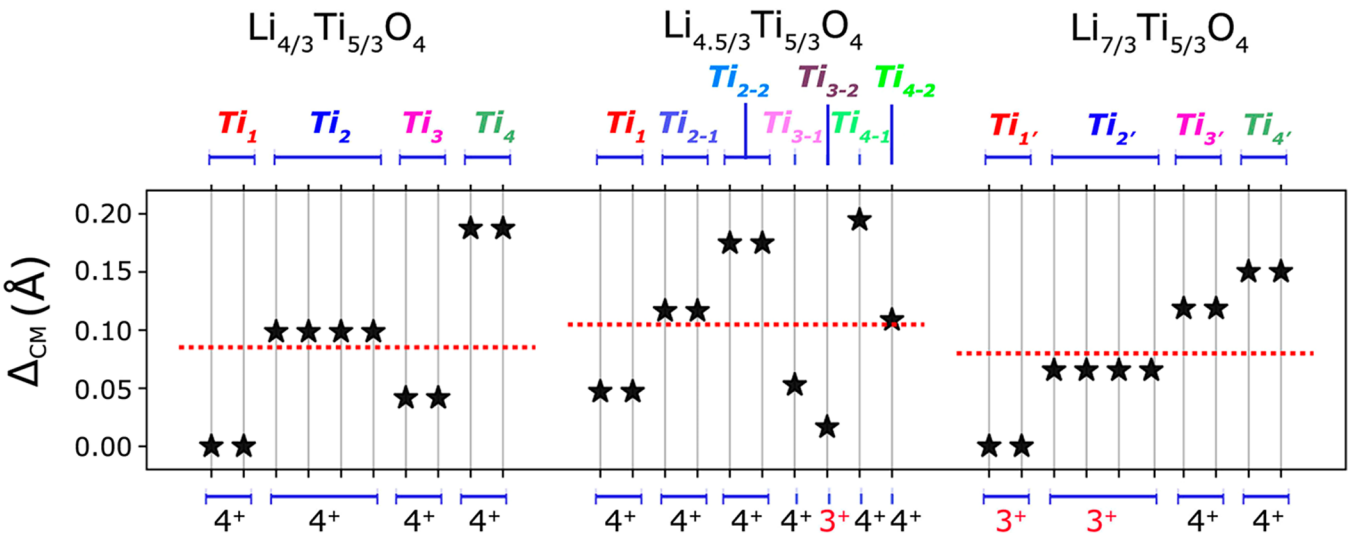

Figure 7. Off-center displacement Δ_{CM} of individual Ti ions in $Li_{4/3}Ti_{5/3}O_4$, $Li_{4.5/3}Ti_{5/3}O_4$, and $Li_{7/3}Ti_{5/3}O_4$. The red dashed lines represent the average Δ_{CM} of each phase due to local distortion, which increased during early lithiation, to $Li_{4.5/3}Ti_{5/3}O_4$, but eventually decreased in the final $Li_{7/3}Ti_{5/3}O_4$. The valence states of different types of Ti ions are labeled for each phase (bottom), corresponding to the structures in Figure 4a.

$Li_{4.5/3}Ti_{5/3}O_4$ and $Li_{7/3}Ti_{5/3}O_4$ are shown in Figure S11. The phenomenon of red-shift in the K-edge of transition metals due to reduction (i.e., the effect of ΔE_{1s}) is commonly reported in literature, such as red-shift in vanadium K-edge spectrum caused by the reduction of V^{5+} to V^{4+} in V_2O_5 during lithiation.[56] Similarly, because the excitation of core electrons of Ti^{3+} requires less energy as a result of stronger screening than in Ti^{4+}, peak D shifts to lower energies. As shown in Figure 5a, ΔE_D for $Li_{7/3}Ti_{5/3}O_4$ is −2.1 eV in *in situ* XAS and −2.5 eV in OCEAN (Figure 5a). Based on Figure S11, the contribution of ΔE_{1s} is about −1.7 eV, and the remaining −0.8 eV mainly arises from the shift of the unoccupied Ti 4p bands (ΔE_{4p}) to lower energy. The shift of Ti 4p states toward the conduction band minimum is also evident in the Ti-p PDOS of Figure 5b. In addition to ΔE_D, peak D of $Li_{7/3}Ti_{5/3}O_4$ gets broadened as in OCEAN and *in situ* spectra. We attribute this to heterogeneity of the valence states of Ti in $Li_{7/3}Ti_{5/3}O_4$ since it is a combination of Ti^{3+} and Ti^{4+}. For $Li_{4.5/3}Ti_{5/3}O_4$, ΔE_D from the experimental spectra is negligible (Figure 5a), indicating a very weak effect of ΔE_{1s}. This trend is qualitatively reproduced in theory with ΔE_D = −0.1 eV, an order of magnitude smaller than that in $Li_{7/3}Ti_{5/3}O_4$. Peak E is not affected significantly upon Li intercalation.

Structural Origin of Pre-peak B. A pronounced spectral change in the calculated Ti K-edge spectrum of $Li_{7/3}Ti_{5/3}O_4$ is the significant decrease of the A_B as compared to $Li_{4/3}Ti_{5/3}O_4$ (Figure 5a). More details were obtained from the simulated K-edge spectrum for each inequivalent Ti in Figure 6a. Specifically, peak areas of $Ti_{1'}$ and $Ti_{2'}$ in $Li_{7/3}Ti_{5/3}O_4$ are significantly reduced from those of Ti_1 and Ti_2 in $Li_{4/3}Ti_{5/3}O_4$, which results from the reduction of Ti^{4+} to Ti^{3+} in $Li_{7/3}Ti_{5/3}O_4$. On the other hand, Ti_4 in $Li_{7/3}Ti_{5/3}O_4$ has the largest peak area among all inequivalent Ti ions. The peak area of $Ti_{4'}$ is also reduced substantially compared to Ti_4, although both have the same valence of 4+. So the change in the valence state alone cannot explain the decrease of the A_B in $Li_{7/3}Ti_{5/3}O_4$, which may largely result from local structural changes eventually caused by the changes in both the Ti valence state and the crystal field between the two phases.

In a perfect TiO_6 octahedron, Ti 1s to e_g dipole transition is symmetry forbidden. The hybridization between e_g and O p orbitals can cause local distortion of the TiO_6 octahedra, which in turn breaks the d-symmetry and enables the dipole transition of Ti 1s to e_g. At finite temperatures, thermal disorder effects can also break the symmetry and give rise to XAS peaks from otherwise dipole forbidden transitions.[67,72] By decomposing the pre-edge region of calculated XAS spectra of inequivalent Ti ions into Gaussian functions, pre-peaks (A, B, and C) were identified as shown in Figure 6a. Significant intensity loss of pre-peak B from $Li_{4/3}Ti_{5/3}O_4$ to $Li_{7/3}Ti_{5/3}O_4$, which was observed in both *in situ* and calculated XAS spectra, can be attributed to the reduced local distortion in TiO_6 octahedra.

A significant contribution of the local distortion comes from non-uniform TiO_6 distortions, in particular with Ti ion displaced from the center of mass (CM). We introduce Δ_{CM} (illustrated in Figure 6b) as a measure of the displacement of Ti ions from the CM of TiO_6 octahedra. Δ_{CM} was calculated for each inequivalent Ti in both $Li_{4/3}Ti_{5/3}O_4$ and $Li_{7/3}Ti_{5/3}O_4$, as shown in Figure 6c. For instance, Ti_1 and $Ti_{1'}$ ions are at the center of octahedra with Δ_{CM} = 0. Δ_{CM} exhibits sizable variations for different TiO_6 octahedra. The average Δ_{CM} of $Li_{4/3}Ti_{5/3}O_4$ (0.085 Å) is larger than that of $Li_{7/3}Ti_{5/3}O_4$ (0.080 Å), indicating the TiO_6 octahedra become more symmetric after lithiation. Since a larger local distortion caused by Δ_{CM} leads to a larger dipole contribution to the A_B, we further define Δ_{area} as the variation of the peak area relative to that at Δ_{CM} = 0 (for Ti_1 and $Ti_{1'}$ ions). It should be noted that the A_B in Ti_1 and $Ti_{1'}$ ions is non-zero, due to the deviation of their TiO_6 from a perfect octahedron. We found a strong linear correlation between Δ_{CM} and Δ_{area}, as demonstrated in Figure 6c; however, the proportionality appears to be system-specific, e.g., different in $Li_{4/3}Ti_{5/3}O_4$ and $Li_{7/3}Ti_{5/3}O_4$, similar to the observation in perovskite materials in ref 67.

At the intermediate range of $0 < x \leq 0.87$, both $\alpha(x)$ and the $\tilde{A}_B$ deviate significantly from the two-phase transformation line as shown in Figure 3. This trend cannot be simply explained by the reduction of Ti^{4+} to Ti^{3+} alone. We further investigated the effects of local distortion on Δ_{CM} caused by the insertion of Li_{16c} in $Li_{4.5/3}Ti_{5/3}O_4$. As shown in Figure 7, Δ_{CM} (Ti^{3+}_{3-2}) is less

DOI: 10.1021/jacs.7b07628
J. Am. Chem. Soc. 2017, 139, 16591−16603

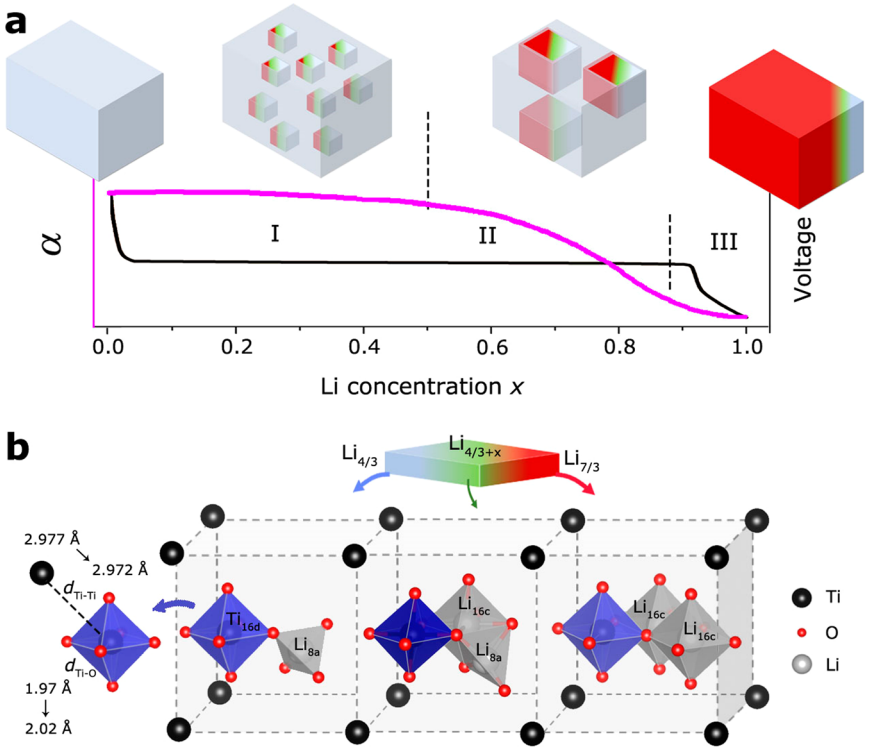

Figure 8. Illustration of the local structural transformations and their correlation to bulk-phase evolution in lithium titanate. (a) Multi-stage structural transformations occurring globally in $Li_{4/3}Ti_{5/3}O_4$ during lithiation: (I) $x = 0-0.50$ (corresponding to high α (weight of pristine $Li_{4/3}Ti_{5/3}O_4$ phase)), where fine $Li_{7/3}Ti_{5/3}O_4$ domains (red) were formed locally inside the pristine $Li_{4/3}Ti_{5/3}O_4$ phase (light blue), along with solid solution phase $Li_{4/3+x}Ti_{5/3}O_4$ (green) at the domain boundaries; (II) $x = 0.50-0.87$ (intermediate α), growth of the $Li_{7/3}Ti_{5/3}O_4$ phase; and (III) $x = 0.87-1.00$ (low α), macroscopic phase separation. (b) Local atomic arrangements in the pristine $Li_{4/3}Ti_{5/3}O_4$, intermediate ($Li_{4/3+x}Ti_{5/3}O_4$), and $Li_{7/3}Ti_{5/3}O_4$ phases, showing the local ordering of cations (Li^+ and $Ti^{3+/4+}$ ions) within the TiO_6 tetrahedra and a large unit cell. Major changes occurred in the Ti−O bonds induced by Li^+ insertion/migration, giving rise to an increase of the average Ti−O distance, d_{Ti-O}, from 1.97 Å ($Li_{4/3}Ti_{5/3}O_4$) to 2.02 Å ($Li_{4/3}Ti_{5/3}O_4$). There is a negligible change in the average Ti−Ti distance d_{Ti-Ti}, from 2.977 Å ($Li_{4/3}Ti_{5/3}O_4$) to 2.972 Å ($Li_{7/3}Ti_{5/3}O_4$).

than Δ_{CM} (Ti^{4+}_{3-1}) by 0.038 Å, and this decrease is in line with the difference of 0.033 Å between Δ_{CM} ($Ti^{3+}_{2'}$) in $Li_{7/3}Ti_{5/3}O_4$ and Δ_{CM} (Ti^{4+}_{2}) in $Li_{4/3}Ti_{5/3}O_4$. In addition to Ti^{4+} reduction, significant local distortions in neighboring TiO_6 octahedra (Ti_{2-2} and Ti_{4-2}) are induced by the face-shared $Li_{8a}/Li_{16c}/Li_{8a}$ motif. In particular, Δ_{CM} (Ti_{2-2}) is larger than Δ_{CM} (Ti_{2-1}) by 0.061 Å. In contrast, Δ_{CM} (Ti_{4-2}) is smaller than Δ_{CM} (Ti_{4-1}) by 0.085 Å. In average, Δ_{CM} in $Li_{4.5/3}Ti_{5/3}O_4$ is slightly larger than that in $Li_{4/3}Ti_{5/3}O_4$ by 0.020 Å. If we assume a same pre-factor between the A_B and Δ_{CM} in $Li_{4/3}Ti_{5/3}O_4$ and $Li_{4.5/3}Ti_{5/3}O_4$ due to their structural similarity, a larger Δ_{CM} implies a larger pre-peak B area or α. In Figure 3, we plotted $\tilde{A}_B$ in OCEAN spectra; data points of $Li_{4.5/3}Ti_{5/3}O_4$ and $Li_{7/3}Ti_{5/3}O_4$ are normalized to that of $Li_{4/3}Ti_{5/3}O_4$. Both experimental and theoretical results show that at the low x region ($x \leq 0.33$), $\tilde{A}_B$ is very close to or slightly above 1.0. Based on our analysis, changes in Δ_{CM} at intermediate range of x are the consequence of the combined effects of Ti^{4+} reduction and local distortion induced by the face-shared $Li_{8a}/Li_{16c}/Li_{8a}$, or more general, Li_{8a}/Li_{16c} motif.

Unlike the computational results in Figure 6c performed at zero temperature, the A_B in Figure 2d was extracted from experimental spectra at room temperature and is subjected to both local structural disorder and thermal disorder. $Li_{4/3}Ti_{5/3}O_4$ has a Debye temperature ($\theta_D = 689 \pm 71$ K) and a small linear bond thermal expansion coefficient ($8.4(4) \times 10^{-6}$ K^{-1}) of Li_{16d}/Ti−O bonds.[73] In ref 67, prior to calculating the average Ti atom displacement in $BaTiO_3$, the peak area of a centrosymmetric perovskite ($EuTiO_3$) was subtracted in order to correct for thermal motion, which was known to have a small peak in the energy region corresponding to the 1s-to-3d transition due to vibrational disorder within the TiO_6 octahedra.[74,75] If we assume the magnitude of the thermal disorder is independent of x, the thermal disorder corrected curve according to ref 67 will have a rigid shift corresponding to smaller A_B, which does not affect the main conclusion of Figure 6c.

In summary, based on excellent agreement between computational and experimental spectra, we were able to identify three key spectral features in Ti K-edge XANES that may be used as fingerprints for tracking structural transformations: (a) the position of main peak D, which is related to the reduction of Ti^{4+} to Ti^{3+}; (b) the emergence of pre-peak S, which is associated with the global migration of Li_{8a} to Li_{16c} and shorter Ti−Li distances; and (c) the area of pre-peak B, which is proportional to the spectral weight of $Li_{4/3}Ti_{5/3}O_4$ and is sensitive to the local TiO_6 distortion. A combination of these spectral fingerprints allows us to unveil the kinetic phase transformation pathway.

Multi-Stage Structural Transformations. As is well established, structural transformation through the solid-solution phase path is favorable for high rate performance,[76−78] since any phase transformation will involve large energy barriers associated with phase nucleation and growth.[79] Structural transformation via solid solution has also been proposed in $Li_{4/3+x}Ti_{5/3}O_4$ by Schmidt and Wilkening.[18] According to their

DOI: 10.1021/jacs.7b07628
J. Am. Chem. Soc. 2017, 139, 16591−16603

report, the electrodes should undergo several stages during lithiation, experiencing a quasi-solid solution initially in local regions, followed by continuous growth of Li-rich regions and eventual transformation into rock-salt type oxide.[18] In the spirit of the model of Schmidt and Wilkening, we propose a multi-stage kinetic model based on quantitative assessment of the structural transformations using *in situ* XANES-based spectral fingerprints, which corresponds to high ($x \leq 0.50$), intermediate ($0.50 \leq x \leq 0.87$), and low α ($0.87 \leq x \leq 1.00$) regions as illustrated in Figure 8.

There are several possible explanations of the remarkable spectral similarity to the initial spinel phase in the first stage. One possibility is that Li ions start to fill the empty 16c sites, while Li ions at 8a sites do not move. This gives rise to a homogeneous $Li_{4/3+x}Ti_{5/3}O_4$ solid-solution phase, as confirmed by the OCEAN spectrum of $Li_{4.5/3}Ti_{5/3}O_4$ with face-shared $Li_{8a}/Li_{16c}/Li_{8a}$ motifs shown in Figure 5a. Alternatively the large deviation from the macroscopic two-phase transformation line in Figure 3 may also be explained by many very fine $Li_{7/3}Ti_{5/3}O_4$ domains (e.g., nm or sub-nm size) with a large interface to volume ratio, so that face-shared Li_{8a}/Li_{16c} motifs at domain boundaries contribute substantially to *in situ* XAS spectra. In this scenario, the pristine phase are expected to be dominant in the form of quasi-solid solution containing many very fine (e.g., nm or sub-nm size) $Li_{7/3}Ti_{5/3}O_4$ domains, as illustrated in Figure 8a. This explains the high spectral weight of the pristine phase in this stage (with $\alpha \geq 0.92$). In addition, the presence of the quasi-solid solution is evidenced by the facts that small shift of peak D (characteristic of solid solution as shown in Figure 5a) is present and the pre-peak S (characteristic of Li ions on 16c sites as shown in Figure 5b) is invisible below $x = 0.5$ (Figure 2b). This observation may be explained by the recent results from theoretical studies, wherein intermediate $Li_{4/3+x}Ti_{5/3}O_4$ with face-shared Li_{8a}/Li_{16c} configurations were found to be energetically favorable at the boundaries of the $Li_{4/3}Ti_{5/3}O_4/Li_{7/3}Ti_{5/3}O_4$ domains, due to the presence of defective Li on Ti sites (octahedral 16d sites).[19] According to the thermodynamic arguments, the thickness of the intermediate $Li_{4/3+x}Ti_{5/3}O_4$ structure is limited to only one or two atomic layers.[19] As a result, at low cycling rates, the quasi-solid solution should be more favorable than the homogeneous solid solution phase because, even if the latter is formed, phase separation will occur, eventually leading to the former case with enough time of relaxation.[13] But when the system is out of the equilibrium, the actual thickness during discharge may depend on the cycling rates, which will in turn affect the structure and Li-ion mobility in the intermediates.

At the range of $0.50 < x \leq 0.87$, it is likely that those local Li-rich regions, with similar configuration as $Li_{7/3}Ti_{5/3}O_4$, start to grow. We expect at this stage Li_{8a} in the solid solution begins to migrate to the 16c sites in a global manner (Figure 8b), as indicated by the emerging of pre-peak S after $x = 0.5$ in Figure 2b. It would lead to the formation of large-sized $Li_{7/3}Ti_{5/3}O_4$ domains (Figure 8a), as indicated the accelerated decrease of the spinel phase ($\alpha(x)$; as shown in Figure 3). Beyond $x = 0.87$, the system follows the two-phase transformation line, with the further growth of $Li_{7/3}Ti_{5/3}O_4$ domains (Figure 8). In this final stage, the amount of solid solution at domain boundaries may become too small to be defected by XANES spectra.

During the lithiation process, significant change occurs in the local structure, and correspondingly, the average Ti−O distance d_{Ti-O} in the TiO_6 octahedra increases from 1.97 Å of $Li_{4/3}Ti_{5/3}O_4$ to 2.02 Å of $Li_{4/3}Ti_{5/3}O_4$ (Figure 4). On the other hand, additional local distortion is introduced in (quasi-) solid solution phase during the early stage of lithiation. As shown in Figure 7, the metastable face-shared $Li_{8a}/Li_{16c}/Li_{8a}$ geometry increases the local distortion of the nearby TiO_6 octahedra, leading to a larger average Δ_{CM} value than that of $Li_{4/3}Ti_{5/3}O_4$. Such local structural fluctuation may be linked to the evolution of the $\tilde{A}_B$ as shown in Figure 3, in which $\tilde{A}_B$ obtained from the calculated spectrum of $Li_{4.5/3}Ti_{5/3}O_4$ is also larger than that of $Li_{4/3}Ti_{5/3}O_4$, which may explain the slight increase of the A_B at $x = 0.13$ (Figure 2d). However, the displacement inside the TiO_6 octahedra does not cause any noticeable change in the Ti sub-lattice, as illustrated in Figure 8b. The change in the Ti−Ti distance is small for all the four types of the Ti ions, and on average, the d_{Ti-Ti} is slightly decreased by 0.005 Å from $Li_{4/3}Ti_{5/3}O_4$ to $Li_{7/3}Ti_{5/3}O_4$ (Figure 4b). Such an observation is consistent with Raman spectroscopy studies, wherein the presence of Li_{16d} ions surrounding the TiO_6 octahedra was found to be crucial to canceling out the local change in the TiO_6 octahedra.[80] Therefore, the structural change is localized within TiO_6 octahedra, leading to the zero-strain characteristics of $Li_{4/3}Ti_{5/3}O_4$.

The formation of the quasi-solid solution phase is also responsible for the quasi-isosbestic point observed in the *in situ* XANES spectra (Figure 2d). The results support the picture that, in addition to the two end-member phases, a quasi-solid solution phase plays a significant role in the intercalation process, which helps to explain the fast Li ion mobility at the intermediate concentrations. Intriguingly, despite that the (quasi)-solid solution phase has distinct structural characteristics from the two end members, its Ti K-edge XANES spectra can still be reproduced with the spectral components of the two end members, highlighting a distinctive core-level spectrum−structure relationship in lithium titanate. Our findings serve as a crucial addition to the existing knowledge of macroscopic two-phase transformation during intercalation in the $Li_{4/3}Ti_{5/3}O_4$ electrode.[8−11,13,15,19]

The observation from *in situ* XAS measurements are in general consistent with the proposed model by Schmidt and Wilkening based on *ex situ* NMR measurement.[18] But it should be noted that kinetic effects may have played an important role in this study, as the materials were functioning under *non-equilibrium* conditions. Therefore, one should not expect the multi-stage structural transformations determined from *in situ* XAS experiments occurred at the same concentration ranges as in ref 18.

This work also demonstrated that *in situ* XANES measurement is highly sensitive to the subtle deviation from pure two-phase transformation in the zero-strain $Li_{4/3}Ti_{5/3}O_4$ system, which is otherwise inaccessible by other methods, such as *in situ* XRD (Figure S3). So the established XANES-based spectral fingerprints may be applied broadly to studies of zero-strain and various other types of electrode materials to obtain quantitative information needed for developing physical models in describing their kinetic electrochemical behaviors.

■ CONCLUSION

In summary, we studied the structural evolution in $Li_{4/3}Ti_{5/3}O_4$ during lithiation through *in situ* XANES measurements combined with *ab initio* simulations. The main spectral features at the pre-edge and the main edge regions were well captured by the theory including the effective electron−core hole interactions. The physical origin of the evolution in these features can be explained by the partial reduction of Ti ions, the

DOI: 10.1021/jacs.7b07628
J. Am. Chem. Soc. 2017, 139, 16591−16603

changes in local distortion of the TiO_6 octahedra and the migration of Li ions. We showed that these spectral fingerprints are sensitive to the amount and location of intercalated Li ions, and hence have a strong correlation to the local structural transformations in lithium titanate, and that effects of local structural change as a result of Li insertion/migration are restricted to the TiO_6 unit, only causing a negligible lattice change in the electrode materials (characteristic of zero strain).

Quantitative spectral weight analysis supports the picture that, in addition to the two end-member phases, the (quasi-) solid-solution phase plays a significant role in the intercalation process, which may explain the fast Li ion mobility at the intermediate concentrations. In contrast to the thermodynamic pathway of phase transformation identified by *ex situ* measurements or theoretical predictions, the identified mechanism of multi-stage structural transformations provides important insights into the kinetic reaction pathway under *non-equilibrium* conditions, which is essential to mechanistic understanding of the performance of the electrodes in LIBs.

The established structure−spectrum correlations may be broadly applicable to *in situ* tracking kinetic pathways of lithium intercalation in zero-strain and other types of electrodes. Furthermore, insights from this study on lithium titanate, a prototype system, may help to pave the way for designing new zero-strain electrodes for long-life batteries.

■ ASSOCIATED CONTENT

Supporting Information

The Supporting Information is available free of charge on the ACS Publications website at DOI: 10.1021/jacs.7b07628.

Results of *in situ* XRD and *ex situ* XAS measurements, detailed information on Gaussian and linear regression fitting of *in situ* XAS spectra, additional calculations on structures, and spectra (PDF)

■ AUTHOR INFORMATION

Corresponding Authors

*amy.marschilok@stonybrook.edu
*dlu@bnl.gov
*fwang@bnl.gov

ORCID

Anatoly I. Frenkel: 0000-0002-5451-1207
Esther S. Takeuchi: 0000-0001-8518-1047
Amy C. Marschilok: 0000-0001-9174-0474
Feng Wang: 0000-0003-4068-9212

Author Contributions

⊗W.Z. and M.T. contributed equally to this work.

Notes

The authors declare no competing financial interest.

■ ACKNOWLEDGMENTS

This work was supported by the Center for Mesoscale Transport Properties, an Energy Frontier Research Center supported by the U.S. Department of Energy, Office of Science, Basic Energy Sciences, under award no. DE-SC0012673. The effort on calculations by M.T. was supported by LDRD Project at BNL (No. 16-039). The effort on interpretation of X-ray absorption by A.I.F. was supported by the U.S. Department of Energy grant no. DE-FG02-03ER15476. The effort on electron microscopy measurements by L.W. and Y.Z. was supported by the U.S. Department of Energy, Office of Basic Energy Science, Division of Materials Science and Engineering, under Contract No. DE-SC0012704. The use of the National Synchrotron Light Source was also supported by the U.S. Department of Energy, Office of Science, Basic Energy Sciences, under Contract No. DE-SC0012704. This research used resources of the Center for Functional Nanomaterials, which is a U.S. DOE Office of Science Facility, at Brookhaven National Laboratory under Contract No. DE-SC0012704. This research used resources of the National Energy Research Scientific Computing Center, a U.S. DOE Office of Science User Facility supported by the Office of Science of the U.S. Department of Energy under Contract No. DE-AC02-05CH11231. We acknowledge Ganesh Venugopal and Andrew Hunt from nGimat for providing $Li_4Ti_5O_{12}$ samples, and fruitful discussions with Drs. Shinjae Yoo (Computational Science Initiative, BNL), John T. Vinson (NIST), Eric L. Shirley (NIST), Yan Li (American Physical Society), Dong-Hwa Seo (University of California; Berkeley), and Joaquim Jaumot (IDAEA-CSIC, Barcelona).

■ REFERENCES

(1) Whittingham, M. S. *Proc. IEEE* **2012**, *100*, 1518.
(2) Dunn, B.; Kamath, H.; Tarascon, J.-M. *Science* **2011**, *334*, 928.
(3) Colbow, K.; Dahn, J.; Haering, R. *J. Power Sources* **1989**, *26*, 397.
(4) Ohzuku, T.; Ueda, A.; Yamamoto, N. *J. Electrochem. Soc.* **1995**, *142*, 1431.
(5) Ferg, E.; Gummow, R.; De Kock, A.; Thackeray, M. *J. Electrochem. Soc.* **1994**, *141*, L147.
(6) Yi, T.-F.; Jiang, L.-J.; Shu, J.; Yue, C.-B.; Zhu, R.-S.; Qiao, H.-B. *J. Phys. Chem. Solids* **2010**, *71*, 1236.
(7) Zaghib, K.; Dontigny, M.; Guerfi, A.; Charest, P.; Rodrigues, I.; Mauger, A.; Julien, C. M. *J. Power Sources* **2011**, *196*, 3949.
(8) Kitta, M.; Akita, T.; Tanaka, S.; Kohyama, M. *J. Power Sources* **2013**, *237*, 26.
(9) Kitta, M.; Akita, T.; Tanaka, S.; Kohyama, M. *J. Power Sources* **2014**, *257*, 120.
(10) Lu, X.; Zhao, L.; He, X.; Xiao, R.; Gu, L.; Hu, Y. S.; Li, H.; Wang, Z.; Duan, X.; Chen, L.; et al. *Adv. Mater.* **2012**, *24*, 3233.
(11) Pang, W. K.; Peterson, V. K.; Sharma, N.; Shiu, J.-J.; Wu, S.-h. *Chem. Mater.* **2014**, *26*, 2318.
(12) Scharner, S.; Weppner, W.; Schmid-Beurmann, P. *J. Electrochem. Soc.* **1999**, *146*, 857.
(13) Wagemaker, M.; Simon, D. R.; Kelder, E. M.; Schoonman, J.; Ringpfeil, C.; Haake, U.; Lützenkirchen-Hecht, D.; Frahm, R.; Mulder, F. M. *Adv. Mater.* **2006**, *18*, 3169.
(14) Schmidt, W.; Bottke, P.; Sternad, M.; Gollob, P.; Hennige, V.; Wilkening, M. *Chem. Mater.* **2015**, *27*, 1740.
(15) Wagemaker, M.; van Eck, E. R.; Kentgens, A. P.; Mulder, F. M. *J. Phys. Chem. B* **2009**, *113*, 224.
(16) Wilkening, M.; Iwaniak, W.; Heine, J.; Epp, V.; Kleinert, A.; Behrens, M.; Nuspl, G.; Bensch, W.; Heitjans, P. *Phys. Chem. Chem. Phys.* **2007**, *9*, 6199.
(17) Hain, H.; Scheuermann, M.; Heinzmann, R.; Wünsche, L.; Hahn, H.; Indris, S. *Solid State Nucl. Magn. Reson.* **2012**, *42*, 9.
(18) Schmidt, W.; Wilkening, M. *J. Phys. Chem. C* **2016**, *120*, 11372.
(19) Ganapathy, S.; Vasileiadis, A.; Heringa, J. R.; Wagemaker, M. *Adv. Energy Mater.* **2017**, *7*, 1601781.
(20) Grey, C.; Tarascon, J. *Nat. Mater.* **2017**, *16*, 45.
(21) Kim, S.; Fang, S.; Zhang, Z.; Chen, J.; Yang, L.; Penner-Hahn, J. E.; Deb, A. *J. Power Sources* **2014**, *268*, 294.
(22) Kartha, J.; Tunstall, D.; Irvine, J. T. *J. Solid State Chem.* **2000**, *152*, 397.
(23) Ronci, F.; Stallworth, P.; Alamgir, F.; Schiros, T.; Van Sluytman, J.; Guo, X.; Reale, P.; Greenbaum, S.; Scrosati, B. *J. Power Sources* **2003**, *119*, 631.

DOI: 10.1021/jacs.7b07628
J. Am. Chem. Soc. 2017, 139, 16591−16603

(24) Ronci, F.; Stallworth, P.; Alamgir, F.; Schiros, T.; Van Sluytman, J.; Guo, X.; Reale, P.; Greenbaum, S.; Scrosati, B. *J. Power Sources* **2003**, *119*, 631.
(25) Farges, F.; Brown, G. E.; Rehr, J. J. *Geochim. Cosmochim. Acta* **1996**, *60*, 3023.
(26) Joly, Y.; Cabaret, D.; Renevier, H.; Natoli, C. R. *Phys. Rev. Lett.* **1999**, *82*, 2398.
(27) Waychunas, G. A. *Am. Mineral.* **1987**, *72*, 89.
(28) Jiang, N.; Su, D.; Spence, J. *Phys. Rev. B* **2007**, *76*, 214117.
(29) Lippens, P.-E.; Womes, M.; Kubiak, P.; Jumas, J.-C.; Olivier-Fourcade, J. *Solid State Sci.* **2004**, *6*, 161.
(30) Wang, F.; Wu, L.; Ma, C.; Su, D.; Zhu, Y.; Graetz, J. *Nanotechnology* **2013**, *24*, 424006.
(31) Venkateswarlu, M.; Chen, C.; Do, J.; Lin, C.; Chou, T.-C.; Hwang, B. *J. Power Sources* **2005**, *146*, 204.
(32) Colin, J. F.; Godbole, V.; Novák, P. *Electrochem. Commun.* **2010**, *12*, 804.
(33) Shu, J. J. *J. Solid State Electrochem.* **2009**, *13*, 1535.
(34) Newville, M. J. *J. Synchrotron Radiat.* **2001**, *8*, 322.
(35) Ravel, B.; Newville, M. J. *J. Synchrotron Radiat.* **2005**, *12*, 537.
(36) Heyd, J.; Scuseria, G. E.; Ernzerhof, M. *J. Chem. Phys.* **2003**, *118*, 8207.
(37) Hummer, K.; Harl, J.; Kresse, G. *Phys. Rev. B* **2009**, *80*, 115205.
(38) Paier, J.; Marsman, M.; Hummer, K.; Kresse, G.; Gerber, I. C.; Ángyán, J. G. *J. Chem. Phys.* **2006**, *124*, 154709.
(39) Kresse, G.; Joubert, D. *Phys. Rev. B* **1999**, *59*, 1758.
(40) Kresse, G.; Hafner, J. *Phys. Rev. B* **1993**, *47*, 558.
(41) Kresse, G.; Hafner, J. *Phys. Rev. B* **1994**, *49*, 14251.
(42) Mattioli, G.; Filippone, F.; Alippi, P.; Amore Bonapasta, A. *Phys. Rev. B: Condens. Matter Mater. Phys.* **2008**, *78*, 241201.
(43) Tanaka, Y.; Ikeda, M.; Sumita, M.; Ohno, T.; Takada, K. *Phys. Chem. Chem. Phys.* **2016**, *18*, 23383.
(44) Cococcioni, M.; De Gironcoli, S. *Phys. Rev. B* **2005**, *71*, 035105.
(45) Selcuk, S.; Selloni, A. *Nat. Mater.* **2016**, *15*, 1107.
(46) Gilmore, K.; Vinson, J.; Shirley, E. L.; Prendergast, D.; Pemmaraju, C. D.; Kas, J. J.; Vila, F. D.; Rehr, J. J. *Comput. Phys. Commun.* **2015**, *197*, 109.
(47) Vinson, J.; Rehr, J.; Kas, J.; Shirley, E. *Phys. Rev. B* **2011**, *83*, 115106.
(48) Giannozzi, P.; Baroni, S.; Bonini, N.; Calandra, M.; Car, R.; Cavazzoni, C.; Ceresoli, D.; Chiarotti, G. L.; Cococcioni, M.; Dabo, I.; et al. *J. Phys.: Condens. Matter* **2009**, *21*, 395502.
(49) Egerton, R. *Micron* **2003**, *34*, 127.
(50) Vinson, J.; Kas, J.; Vila, F.; Rehr, J.; Shirley, E. *Phys. Rev. B* **2012**, *85*, 045101.
(51) Leriche, J.; Hamelet, S.; Shu, J.; Morcrette, M.; Masquelier, C.; Ouvrard, G.; Zerrouki, M.; Soudan, P.; Belin, S.; Elkaïm, E.; et al. *J. Electrochem. Soc.* **2010**, *157*, A606.
(52) Yoon, W.-S.; Chung, K. Y.; McBreen, J.; Zaghib, K.; Yang, X.-Q. *Electrochem. Solid-State Lett.* **2006**, *9*, A415.
(53) Lawson, C. L.; Hanson, R. J. *Solving Least Squares Problems*; SIAM: Philadelphia, 1995.
(54) Conti, P.; Zamponi, S.; Giorgetti, M.; Berrettoni, M.; Smyrl, W. H. *Anal. Chem.* **2010**, *82*, 3629.
(55) Jaumot, J.; de Juan, A.; Tauler, R. *Chemom. Intell. Lab. Syst.* **2015**, *140*, 1−12.
(56) Horrocks, G. A.; Braham, E. J.; Liang, Y.; De Jesus, L. R.; Jude, J.; Velázquez, J. M.; Prendergast, D.; Banerjee, S. *J. Phys. Chem. C* **2016**, *120*, 23922.
(57) Ziebarth, B.; Klinsmann, M.; Eckl, T.; Elsässer, C. *Phys. Rev. B* **2014**, *89*, 174301.
(58) Zhang, W.; Seo, D.-H.; Wu, L.; Topsakal, M.; Lu, D.; Zhu, Y.; Ceder, G.; Wang, F., manuscript in preparation.
(59) Perdew, J. P.; Burke, K.; Ernzerhof, M. *Phys. Rev. Lett.* **1996**, *77*, 3865.
(60) Duan, H.; Li, J.; Du, H.; Chiang, S. W.; Xu, C.; Duan, W.; Kang, F. *J. Phys. Chem. C* **2015**, *119*, 5238.
(61) Tsai, P.-c.; Hsu, W.-D.; Lin, S.-k. *J. Electrochem. Soc.* **2014**, *161*, A439.
(62) Zhong, Z.; Ouyang, C.; Shi, S.; Lei, M. *ChemPhysChem* **2008**, *9*, 2104.
(63) Verde, M. G.; Baggetto, L.; Balke, N.; Veith, G. M.; Seo, J. K.; Wang, Z.; Meng, Y. S. *ACS Nano* **2016**, *10*, 4312.
(64) Bhattacharya, J.; Van der Ven, A. *Phys. Rev. B* **2010**, *81*, 104304.
(65) Woicik, J.; Shirley, E. L.; Hellberg, C.; Andersen, K.; Sambasivan, S.; Fischer, D.; Chapman, B.; Stern, E.; Ryan, P.; Ederer, D.; et al. *Phys. Rev. B* **2007**, *75*, 140103.
(66) Itié, J.; Couzinet, B.; Polian, A.; Flank, A.; Lagarde, P. *EPL (Europhys. Lett.)* **2006**, *74*, 706.
(67) Frenkel, A.; Feldman, Y.; Lyahovitskaya, V.; Wachtel, E.; Lubomirsky, I. *Phys. Rev. B* **2005**, *71*, 024116.
(68) Shirley, E. L. J. *J. Electron Spectrosc. Relat. Phenom.* **2004**, *136*, 77.
(69) Cocchi, C.; Zschiesche, H.; Nabok, D.; Mogilatenko, A.; Albrecht, M.; Galazka, Z.; Kirmse, H.; Draxl, C.; Koch, C. T. *Phys. Rev. B* **2016**, *94*, 075147.
(70) Vinson, J.; Jach, T.; Müller, M.; Unterumsberger, R.; Beckhoff, B. *Phys. Rev. B* **2016**, *94*, 035163.
(71) Liang, Y.; Vinson, J.; Pemmaraju, S.; Drisdell, W. S.; Shirley, E. L.; Prendergast, D. *Phys. Rev. Lett.* **2017**, *118*, 096402.
(72) England, A. H.; Duffin, A. M.; Schwartz, C. P.; Uejio, J. S.; Prendergast, D.; Saykally, R. J. *Chem. Phys. Lett.* **2011**, *514*, 187.
(73) Dolotko, O.; Senyshyn, A.; Mühlbauer, M. J.; Boysen, H.; Monchak, M.; Ehrenberg, H. *Solid State Sci.* **2014**, *36*, 101.
(74) Ravel, B. Ph.D. Thesis, University of Washington, 1995.
(75) Kraizman, V.; Novakovich, A.; Vedrinskii, R.; Timoshevskii, V. *Phys. B* **1995**, *208*, 35.
(76) Liu, H.; Strobridge, F. C.; Borkiewicz, O. J.; Wiaderek, K. M.; Chapman, K. W.; Chupas, P. J.; Grey, C. P. *Science* **2014**, *344*, 1252817.
(77) Xia, Y.; Sakai, T.; Fujieda, T.; Yang, X.; Sun, X.; Ma, Z.; McBreen, J.; Yoshio, M. *J. Electrochem. Soc.* **2001**, *148*, A723.
(78) Yabuuchi, N.; Ohzuku, T. *J. Power Sources* **2003**, *119*, 171.
(79) Malik, R.; Zhou, F.; Ceder, G. *Nat. Mater.* **2011**, *10*, 587.
(80) Mukai, K.; Kato, Y.; Nakano, H. *J. Phys. Chem. C* **2014**, *118*, 2992.

DOI: 10.1021/jacs.7b07628
J. Am. Chem. Soc. 2017, 139, 16591−16603